

Test Solenoids
Expected Performance and Test Results
Part I: PDST01-0 and PDST01-1

R. Carcagno, C. Hess, F. Lewis, D. Orris, Y. Pischalnikov, R. Rabehl,
M. Tartaglia, I. Terechkine, J. Tompkins, T. Wokas

This note describes results obtained during testing of the so-called “test solenoid”. In total there are three test solenoids built using different superconducting strand: PDST01, 02, and 03. All coils were wound with the tension of ~ 20 N with layers separated by fiberglass cloth, then vacuum impregnated with epoxy. The main geometrical parameters are the same for all the three. A sketch of the test solenoid assembled with the flux return is shown in Fig. 1. PDST01 was tested during March and April of 2006 in two configurations: PDST01-0 refers to the “bare” solenoid, while PDST01-1 refers to the solenoid with the flux return; PDST02 and PDST03 were both tested without yoke, and results are reported in separate notes.

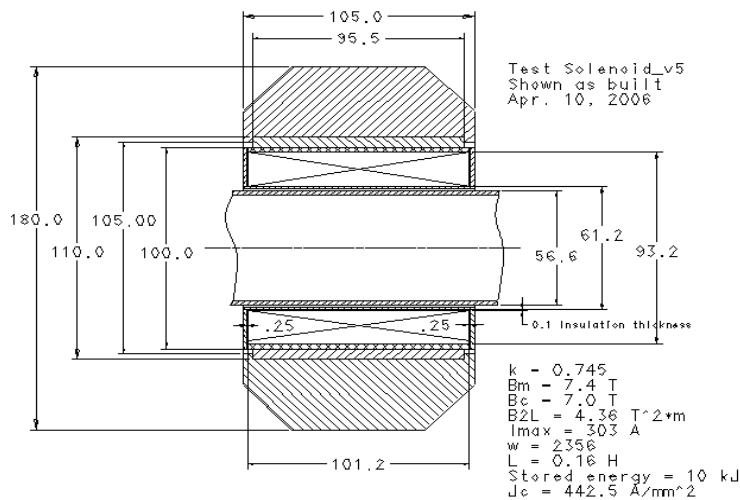


Fig. 1: Test solenoid as built. The coil outer diameter can vary by ± 0.5 mm.

I. PDST01-0 – Coil Without a Flux Return

Geometrical Parameters of the Coil (winding only; insulation thickness not included)

D_i	= 61.2 mm	Inner Diameter
D_o	= 93.2 mm	Outer Diameter
l	= 101 mm	Coil Length
N	= 2355.7	Number of turns in the coil
R	= 32 Ohm	Coil resistance at Room Temperature
L	= 150 mH	Coil inductance (without Iron Yoke)

Strand Parameters

NbTi strand for the coil has been provided by LBNL that manages the leftover stock from the SSC project. It was developed for the inner coil of the SSC HEB dipole. This strand was developed to meet two types of specifications and several vendors participated

in this project, so the type of the strand was identified only after analyzing its cross-section and comparing it with available data of different vendors. The counted number of filaments and the “measured” strand diameter pointed to the “new” strand specification and IGC as a vendor of the strand. Strand parameters are shown in the table below:

Cu /nonCu ratio	1.5
Bare strand diameter, d	0.808 mm
Effective filament diameter	6 μm
Number of filaments	~ 8000

Coil Compaction Factor

Coil compaction (packing) factor defines density of winding and is a ratio of the total cross-section of bare strand in the winding to the winding cross-section. For PDST01,

$$k = [N \pi d^2 / 4] / [l*(Do - Di)/2] = \mathbf{0.746}$$

Quench Current and Field Strength

Magnetic modeling resulted in the next set of expected solenoid parameters:

Iq = 307.5 A	Quench Current at 4.2K
Bc = 7.1 T	Central field at Quench
Bm = 7.5 T	Maximum field in the coil
Eff = 0.02314 T/A	Solenoid efficiency, Bc / Iq

The evaluation of the coil performance was made by using the strand performance measured in the TD short sample test facility [1] that can be expressed by the formula:

$$I_c = 440 - 129.6*(B - 6.5)$$

$$\text{or } B_c = 9.895 - I/129.5$$

The strand quench behavior was slightly better than required by the SSC inner strand specification [2] resulting in slightly higher quench current than would be otherwise expected (302.6 A). The expected quench current must be adjusted for the temperature difference during testing of the strand (4.2 K) and the solenoid (4.35 K - boiling helium at 16 PSIA). Fig. 2 shows the strand critical current for the two temperatures: Ic1(B) for 4.2 K (in red) and Ic2(B) for 4.35 K (blue). The superimposed solenoid load line Iload(B) allows finding the critical field and current. The graph predicts about 2% lower quench current at 4.35 K and brings the expected quench current to ~ 302.2 A.

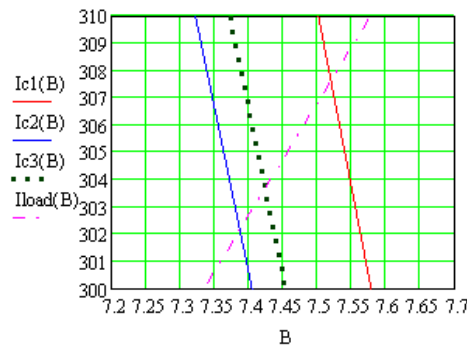


Fig. 2: Performance of 0.808 mm SSC strand at different temperatures and adjustment for the increased magnetic field on the strand during strand testing

Another factor to take into account is the accuracy of strand quench current measurement. Analysis of errors is described in [1] and does not include the effect of strand self-generated magnetic field. The additional magnetic field at the strand surface is ~ 0.15 T ($\sim 2\%$) at 305 A for the 0.81 mm strand (see Fig. 3). This results in a corresponding increase of the expected critical current of the solenoid up to ~ 304 A (dotted curve I3(B) in Fig. 2).

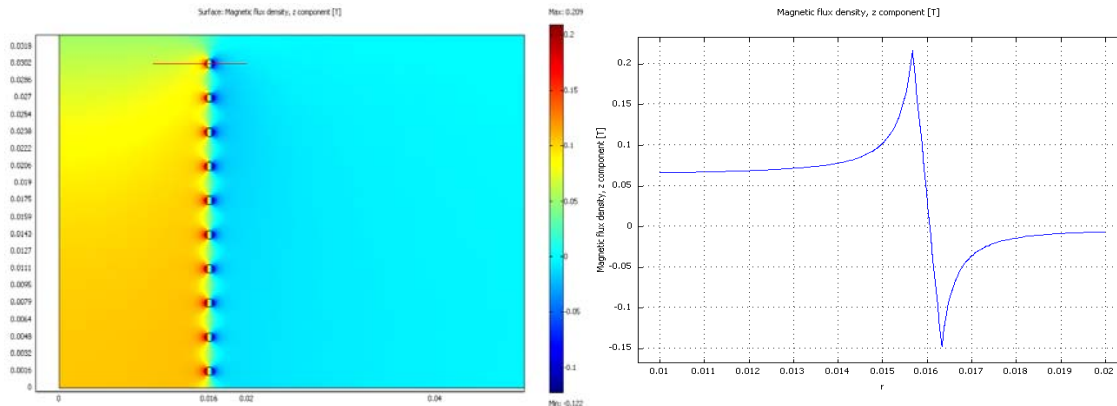


Fig. 3: Magnetic field map in the vicinity of the tested strand (left) and strength profile (right) along the indicated line through a strand on the strand sample holder

Table 1 shows the quench training history during the first and second thermal cycles, between which the solenoid was warmed up to room temperature. In both cases there is clearly no training (consistency within $<0.5\%$) and no obvious dependence of the quench current on the ramp rate. Having just carefully estimated the expected quench current, it is important also to discuss the accuracy of the measured quench currents. The average recorded TC2 current is about 1% higher than in TC1, probably due to changes that were made in the way the magnet current was distributed and digitized early in the test stand commissioning, between the two cold tests. The tabulated currents are slightly underestimated by the MATLAB analysis program: the current drops (by 0.8 A) as the quench develops, but is reported at the time of crossing detection threshold. The Labview quench current is systematically 0.6 A below the unix current. Taking these into account, the measured quench currents are about 1.5% higher than the expected value of ~ 304 A. Further work is planned to determine the absolute accuracy of the measured quench currents, but the quench and magnetic strength data suggest measurement errors are on the order of $\sim \pm 1\%$.

Table 1. PDST01-0 quench currents during “training” in two thermal cycles

TC1			TC2		
Quench #	Ramp Rate [A/s]	I _q [A]	Quench #	Ramp Rate [A/s]	I _q [A]
1	1	305.4	1	2	307.4
2	1	305.3	2	2	305.0
3	1	304.2	3	2	306.8
4	2	305.4	4	4	308.2
5	4	304.7	5	8	306.2

Magnetic Measurement Setup

The magnetic field strength was measured parallel to and along the axis of the test solenoid using a one-axis Hall probe (LPT-141-7s) and Group3 Digital Tesla-meter (DTM-141). The probe was mounted in a stainless steel tube sized to be a close fit within a warm bore and centered on the solenoid axis. This tube was mounted on a motion stage to provide vertical motion along the solenoid axis, with digital position readout ($\sim 0.2\text{mm}$ precision and reproducibility). During cold testing, the inner warm bore temperature was stable and reasonably warm at about 18°C . Measurements were captured both warm and cold, first with the bare solenoid (PDST01-0) and again after the annealed steel flux return was added (PDST01-1).

Two independent power supplies were utilized to excite the coil: a Kepko (40V, 12A) bipolar power supply with precision shunt resistor for measuring current, and Lakeshore (500A) power system with Danfysk current transducer. The Lakeshore system was bipolar up to 125A, but diodes were installed for operation above that current to protect the power supplies. Currents were digitized and recorded independently by two systems: a National Instruments ADC with Labview readout program (used in conjunction with Labview Hall Probe readout program), and a VME/Unix based scan system (standard MTF data acquisition architecture) utilizing a HP3458 (24-bit) DVM programmed to integrate over one line cycle. The Labview-based current readout suffered from a number of difficulties, such as noise and saturation, during this first system test; magnetic measurement results are primarily based upon the Unix readout, which is precise to 0.1% over the range of currents used. A follow-up calibration is anticipated to verify the absolute response and accuracy of transducer, by using a precision shunt resistor. The Hall probe response has been cross-checked against an NMR probe in the 1-2 T field range, and was found to be accurate to 0.1% (a separate TD Note is in preparation).

Magnetic Field Profile

The expected magnetic field profile was found assuming the nominal solenoid geometrical parameters given earlier. Rough profile measurements ($\sim 20\text{ mm}$ steps) using a Hall probe are in reasonable agreement with the expected shape, normalized to the peak field as shown in Fig. 4.

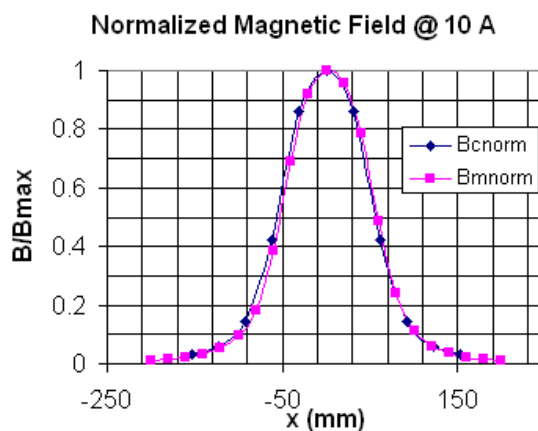


Fig. 4: Comparison of the calculated (B_c norm) and measured (B_m norm) field profiles; the X-position of the peak central field is arbitrary.

Heater-Induced Quench Tests

The heater design, modeling results and some room temperature tests are described in [3]. Two sets of tests were performed on PDST01 to map out the time for coil quenches to develop: first, the coil quench delay was found as a function of the coil current at fixed voltage of the heater firing unit (HFU); second, at a given coil current the coil quench delay was found as a function of the charge voltage of the HFU. The capacitance of the HFU energy storage capacitor was set to 2.4 mF. Four MINCO HK5577 heaters (4.9 Ohm resistance) were connected in a way described in [3]. Because the minimum voltage of the HFU was about 58 V, a 4 Ohm resistor was added in parallel to the heaters to increase the dynamic range of the setup. The total measured resistance of the circuit (including the leads) was 5.9 Ohms. The equivalent load to the HFU was thus 2.38 Ohm and the expected HFU discharge time constant was $\tau = 5.7$ ms. The measured time constant was 5.8 ms; a typical heater voltage pulse shown in Fig. 5 below.

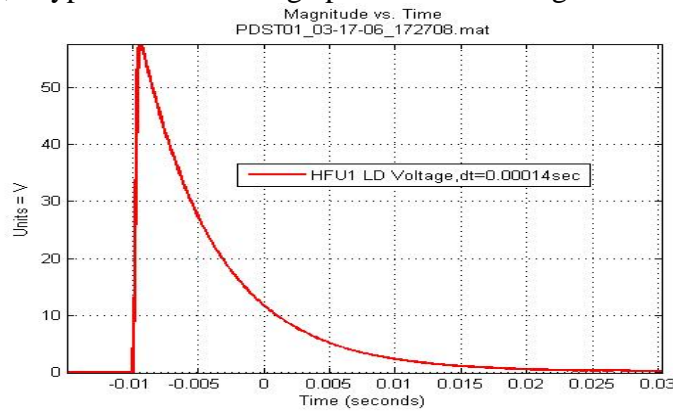
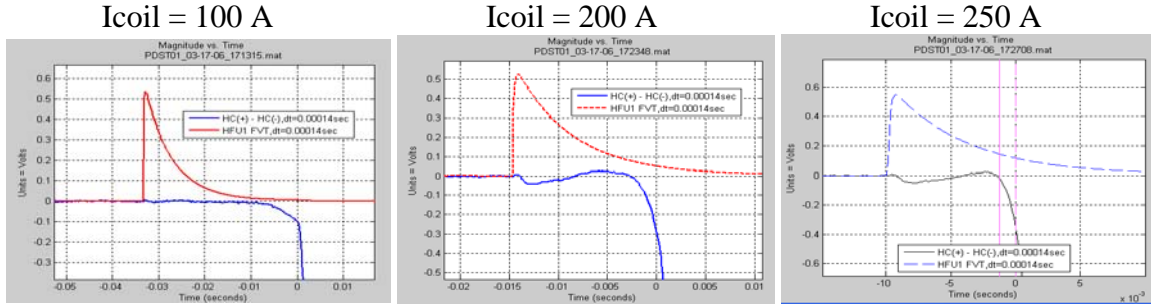


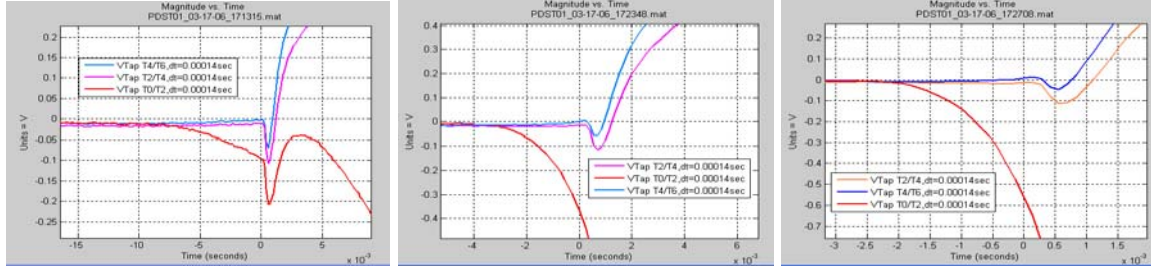
Fig. 5: Typical voltage pulse of the HFU

Knowing the heater circuit parameters, it is possible to evaluate the heater power deposition. At the lowest available HFU voltage, the peak current through the solenoid heaters is $(58 \text{ V} / 5.9 \text{ } \Omega) = 9.8 \text{ A}$, so the current through each heater is 4.9 A. The peak power dissipated by each heater is then $P = I^2 R = 117 \text{ W}$. The active surface of each heater is 250 mm^2 and the total heater area is 500 mm^2 . This allows finding the maximal and average specific power of the heater: 0.47 W/mm^2 and 0.23 W/mm^2 correspondingly. Assuming exponential current profile (Fig 5) the total energy deposition is $W = \frac{1}{2} I^2 R \cdot \tau$. This means that the energy deposited in each heater is $\sim 0.34 \text{ J}$ or $1.35 \cdot 10^3 \text{ Joules}$ per square meter of active heater surface.

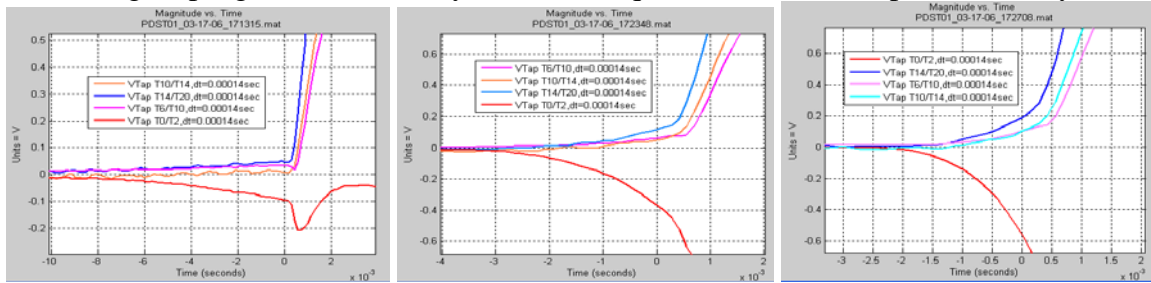
It was impossible to quench the coil using the minimal charging voltage of the HFU when the solenoid current level was below 50 A. At higher excitation levels, the coil quenched. By analyzing the voltage tap quench signal patterns, it is possible to compare results of this heater study with what was predicted during the preliminary stage of this work [3]. Figures 6 “a”, “b”, and “c” show the half-coil difference signals, and voltage tap signals for different current levels in the coil.



6a) HFU pulse and the differential half-coil signal indicating quench



6b) Voltage tap signals for inner layers with the quench in the inner (peak field) layer



6c) Voltage tap signals for the outer layers with the quench in the inner (peak field) layer

Fig. 6: Quench characterization voltage tap signals

These graphs provide the following information:

1. Clearly, the quench starts in the inner layers (voltage tap T0-T2 shows resistive behavior after the heater firing unit is activated).
2. No superconductor-to-normal transition is observed for other layers (the quench protection system activates before the quench propagates)
3. The quench delay depends on the current level, and changes from $\sim 26\text{ ms}$ at 100 A to $\sim 12\text{ ms}$ at 200 A , to $\sim 8\text{ ms}$ at 250 A

The second set of data was captured at a given coil current ($\sim 250\text{ A}$), but changing the heater energy deposition by adjusting voltage of the Heater Firing Unit (HFU). Following a similar analysis to that shown above, we extract the dependence of the quench onset versus voltage of the HFU. Fig. 7 below presents this graph in comparison with the expected delay calculated using the method described in [3] with the total insulation thickness of $\sim 150\text{ }\mu\text{m}$.

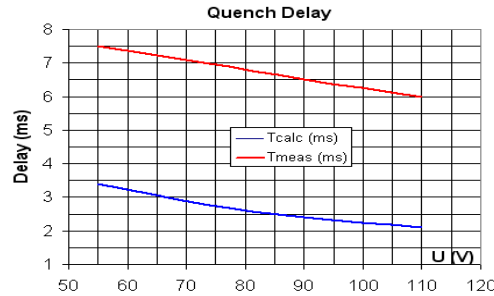


Fig. 7: Quench onset delay as a function of the HFU charging voltage.

There is some difference between the measured and the predicted delays. This difference can be understood by taking into the account the uncertainty of the insulation thickness between the active part of the heater and the nearest strand. Investigation showed that a recession in the cylindrical bobbin for placement of the heaters was a bit deeper than was required, resulting in increased thickness of insulation; also, an air gap could develop between the layers of insulation that would significantly compromise heat transfer.

Further reduction of the delay is still possible by increasing the HFU voltage. The natural limit here is the temperature of the active part of the heater. Fig. 8 shows the dependence of heater temperature on the HFU voltage. Although there is some reserve in the temperature, at this point we decided not to put the device at risk by increasing the HFU voltage.

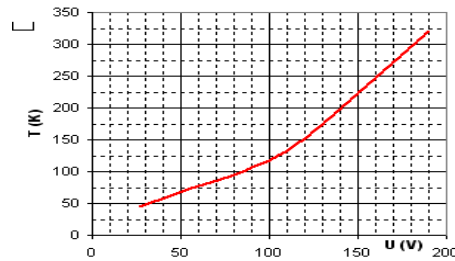


Fig. 8: Heater temperature as function of the HFU charging voltage

DC Power Deposition Test

Because the solenoids are to work in the environment of a beam line with possible beam losses, it was useful to apply a DC voltage to the heaters to simulate additional heating from beam power loss. Corresponding tests were made with two levels of the coil current (which bracket the expected operating point): 200 A and 250 A. At 250 A, the total power in the heaters reached 1.4 W before quench occurred, and at 200 A this power reached 2.8 W. Because this power was deposited on the outer surface of the bobbin (just below the coil inner winding), and concentrated at the heaters, the real ability of the solenoid to withstand thermal loads due to beam loss will be probably better.

Solenoid Survival Test

The test was made to check whether the solenoid was self-protected, that is whether it was safe to let all the energy stored in the magnetic field dissipate in the coil. During this test, the dump resistor circuit, that usually was used to externally dissipate a significant fraction of the stored energy, was disabled. So, all the energy was dissipated by the coil windings that turned (at least partially) normal. Two successive full energy deposition

events were recorded, followed by a ramp to 300 A with no quench, that have shown that the test solenoid is self-protected.

Analyzing the diagrams generated during coil quenching, it was possible to extract information about quench propagation and compare the results with predictions of the modeling described in [4] and [5]. The first important observation made was that the current shape after quench was quite close to that calculated in [5], as shown in Fig. 9. During the initial ($t < 0.25$ s) development, the two curves are almost identical. At the tail of the curve, the measured current shows faster decay. The average current decay time constant is 0.13 sec for the central part of the curve, corresponding to a coil resistance of ~ 1.2 Ohm and is quite consistent with the result obtained in [5] (see Fig. 18 in [5]).

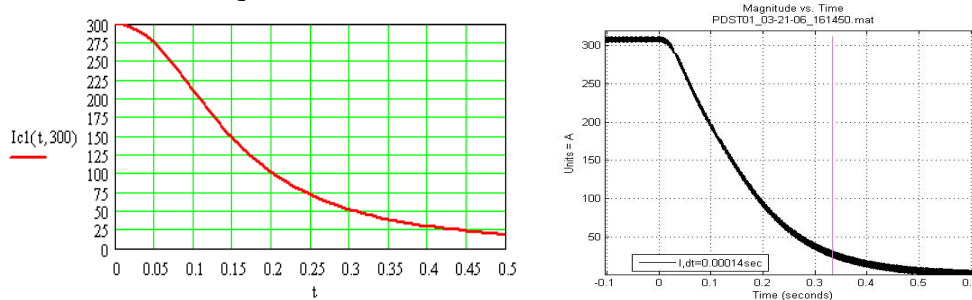


Fig. 9: The measured and the predicted current in the solenoid during quenching.

This behavior gives a hint that the quench propagation process described in [4] is quite close to what actually occurs. Better understanding of this can be obtained by analyzing the voltage tap signals, which are similar to those shown in Fig. 6 above. Table 2 summarizes the results of this analysis showing delays for resistive voltage to develop in different layers of the solenoid.

Table 2. Quench development times versus coil layer, from voltage tap signals

Layer numbers	Quench onset at 308 A (ms)
1-2	0
3-4	3
5-6	7
7-10	25
11-14	40
15-20	No records

These measured quench propagation delays, from inner to outer regions of the coil, can be compared with the diagram in Fig.21-c of [4] corresponding to the current 330 A. According to these diagrams, the quench reaches the middle part of the coil after ~ 12 ms (~ 25 ms measured); all the coil quenches at ~ 44 ms ($> \sim 40$ ms measured). So, we can conclude here that the modeling provides us with quite an adequate picture of quench propagation.

Stress in the Solenoid

The solenoid was equipped with two “active” strain gauges (VISHAY, Micro-Measurement Group, WK-09-250BG-350/W) located in the bore to measure azimuthal strain in the pipe on which the coil was wound. Strain data were collected during the whole process of the solenoid assembly. The thermal response of the gauges was measured prior to solenoid assembly, and is shown in Fig. 10 in comparison with vendor’s data (“thermal output” in vendor-defined units, related to gauge resistance):

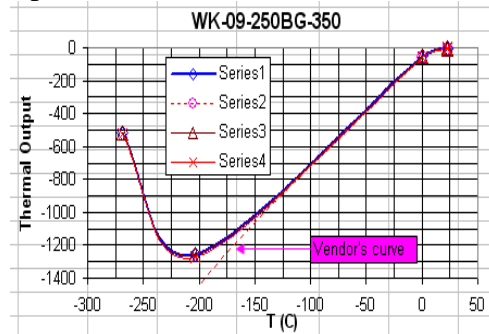


Fig. 10: Strain gauge thermal calibration, compared to vendor data (80K and above)

The accumulation of stress during winding should be visible; however, strain data obtained during winding were very noisy (Fig. 11), suggesting that perhaps the cylindrical winding bobbin was somewhat elliptical.

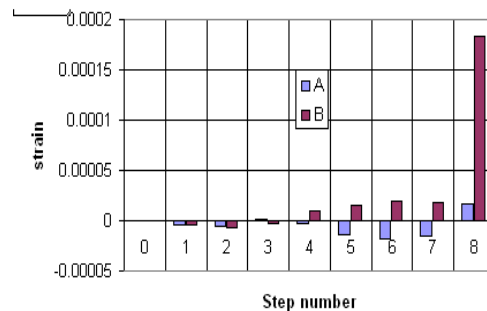


Fig. 11: Strain data during coil winding

Behavior of gauges during cool down compared well with what was measured during the pre-fabrication thermal calibration. In Fig. 12, A and B are the “active” gauges attached to the inner side of the He vessel pipe, CA and CB are “witness” gauges attached to similar stainless steel pipe without winding above it.

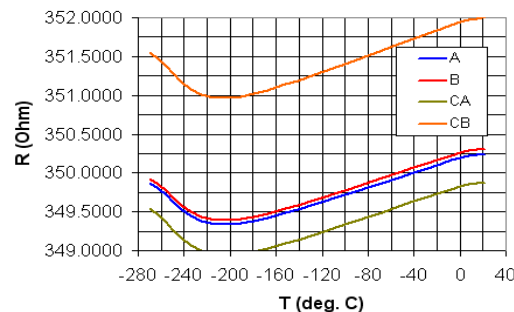


Fig. 12: Gauge measurements during cooling down

After the coil is wound the bobbin is under compression in the radial and azimuthal directions. During excitation, electromagnetic force causes relaxation of the compressive stress/strain in the inner pipe of the He vessel. The measured active gauge resistances change linearly with I^2 , pointing to the electromagnetic nature of the force, as can be seen from Fig. 13a. For both active gauges under the winding, one can see change of the strain. In contrast, the witness strain gauges do not show any signs of change (Fig. 13b).

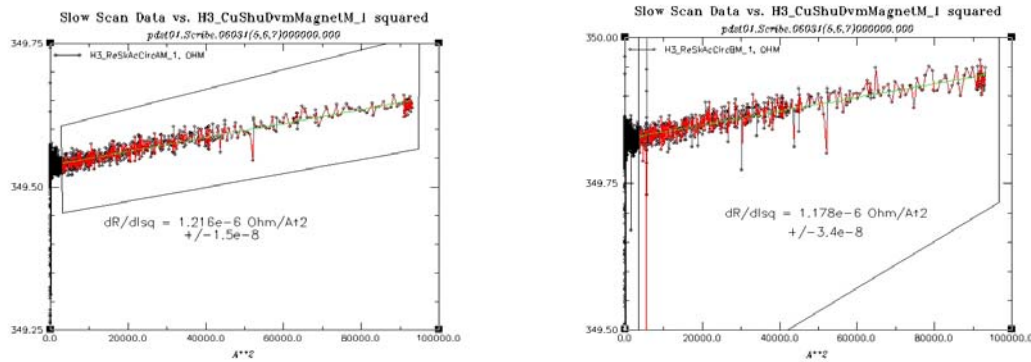


Fig. 13a: Active strain gauge resistance change during excitation

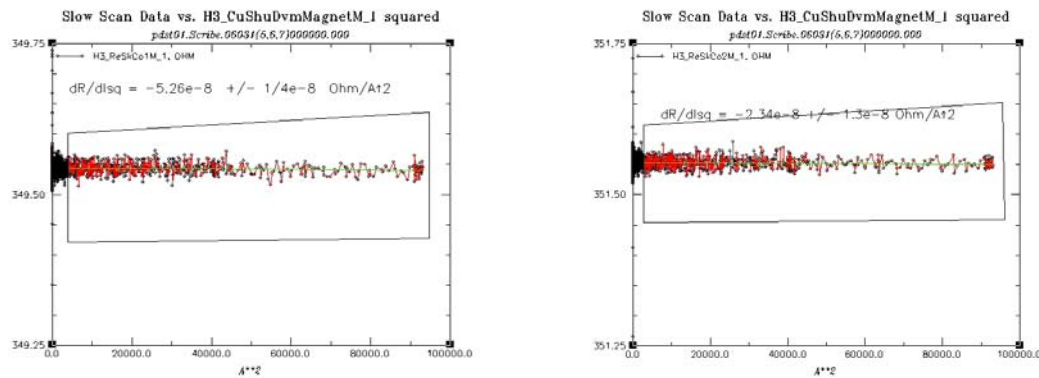


Fig. 13b: Witness strain gauge resistance change during excitation

In Fig. 14, the fractional change in active gauge resistance is converted to strain and, applying the manufacturer's gauge factor, to stress in MPa, showing the parabolic dependence on solenoid current. The level of observed stress is in reasonable agreement with that calculated in [6].

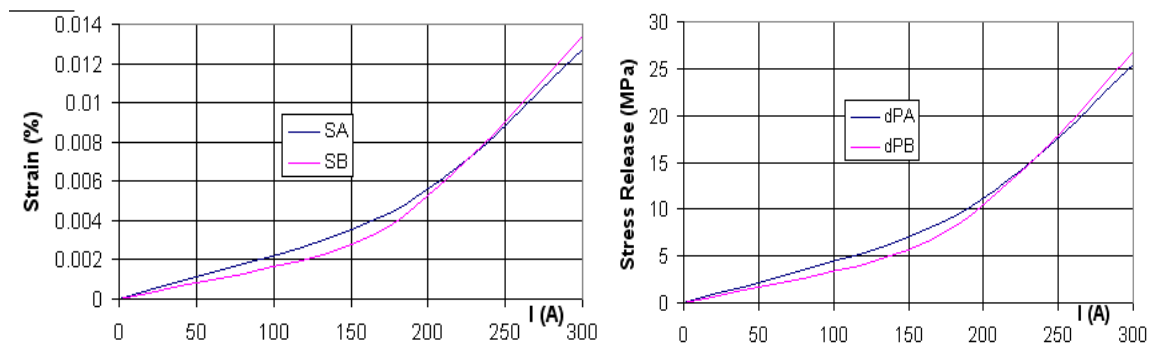


Fig. 14: Behavior of Strain and Stress during the coil excitation cycle

II. PDST01-1 – Coil with the Iron Flux Return Yoke

Modeling

The use of a flux return yoke changes the magnetic field distribution in the test solenoid, which results in slightly different quench point. Because of the presence of the yoke, FE modeling was used that took into account nonlinear effects. Using OPERA module of TOSCA package and COMSOL E/M module with the assumption of typical soft steel permeability gave close results. Fig. 15 shows the cut through the critical surface at 4.2 K and the solenoid load line, which predicts a quench current of 288.1 A. It is necessary to note here that during this test LHe temperature was 4.22 K, so no correction was needed to adjust for the short sample test temperature. No correction for the strand self-field was made at this point.

PDST01-1 Quench Diagram

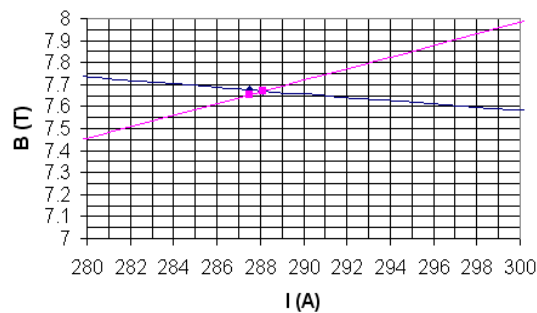


Fig. 15: PDST01-1 calculated critical surface and load line cross at quench current

The magnetic field distribution shown in Fig. 16 indicates that the flux return is highly saturated (at quench current), yet it still concentrates the flux near the coil. Although the iron core becomes saturated, the central field is linear within 0.4% all the way towards the quench current.

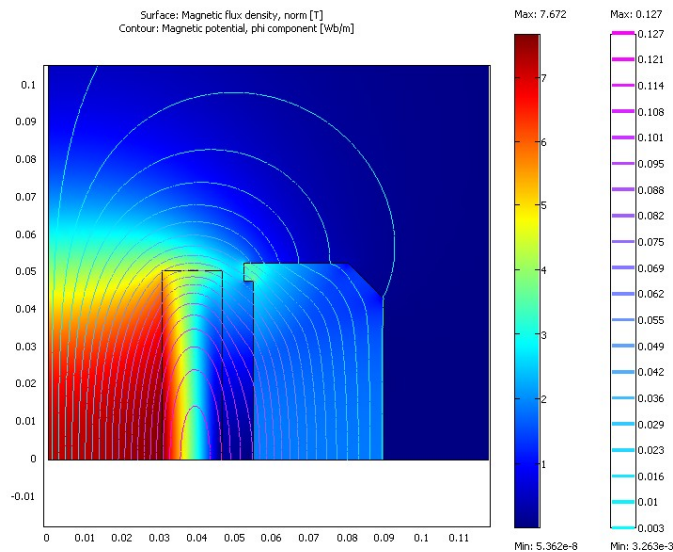


Fig. 16: Magnetic flux density in the vicinity of the solenoid with flux return

Fig. 17 shows that the addition of a flux return makes the field decay faster. This is especially true for the field in the transverse plane, shown in Fig. 18 for the stray field at radial distances beyond the iron yoke.

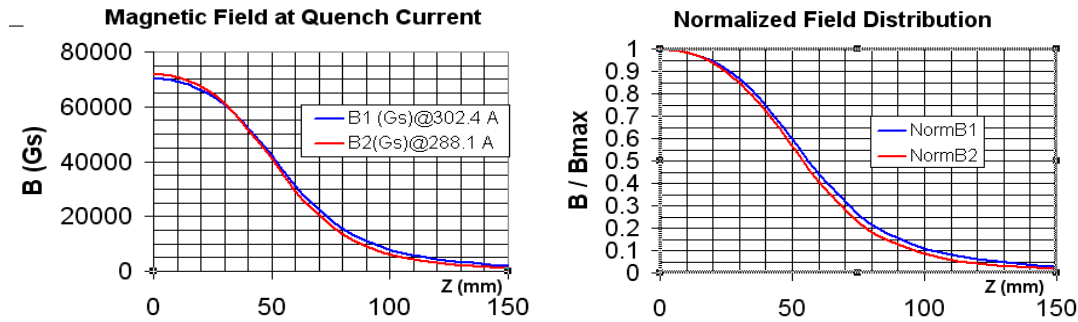


Fig. 17: Calculated axial distribution of magnetic field with (B2) and without (B1) yoke

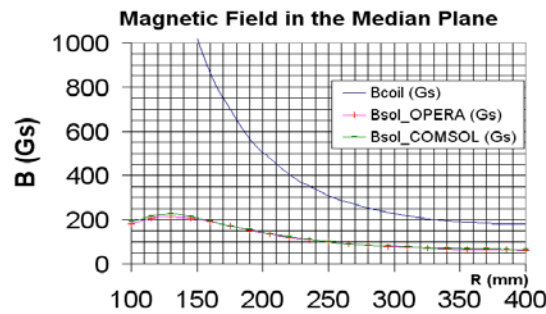


Fig. 18: Comparison of the calculated magnetic field distributions in the transverse plane.

The measured axial field distribution with flux return shows good agreement compared to the predicted shape (Fig. 19).

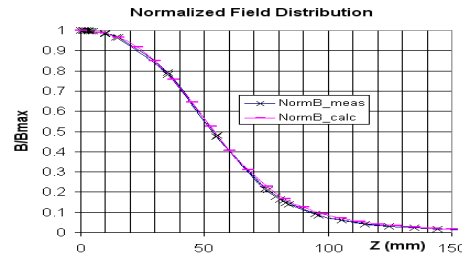


Fig. 19: Normalized calculated and measured field distribution for yoked solenoid

Quench Current

The quench current history for the PDST01-1 is shown in Table 3. The maximal spread of the quench current around its average value (291.8 A) was $\sim 0.2\%$. PDST01-1 was tested at 4.22 K; adjustment for self-field raises the expected quench current (288 A) by $\sim 0.5\%$ to 289.6 A, which is 0.8% below the measurement.

Table 3. PDST01-1 quench currents

Quench #	Ramp Rate [A/s]	Quench Current [A]
1	2	291.6
2	4	292.3
3	8	291.4

Magnetic Field Strength and Measurement System Investigation

The magnetic field profiles along the solenoid axis were measured both warm and cold, for the bare and yoked solenoid. Measured and predicted shapes for the cold solenoid were shown earlier in Fig. 4 and Fig. 19 and the results of the comparison were mostly satisfactory. However, details of the field strength required further understanding. The transfer function, B/I (G/A), is plotted in Fig. 20 (bare and yoked) as a function of magnet current. In all cases, an unexpected variation with current was seen for the transfer function, which reached a plateau at high current, above about 40 A.

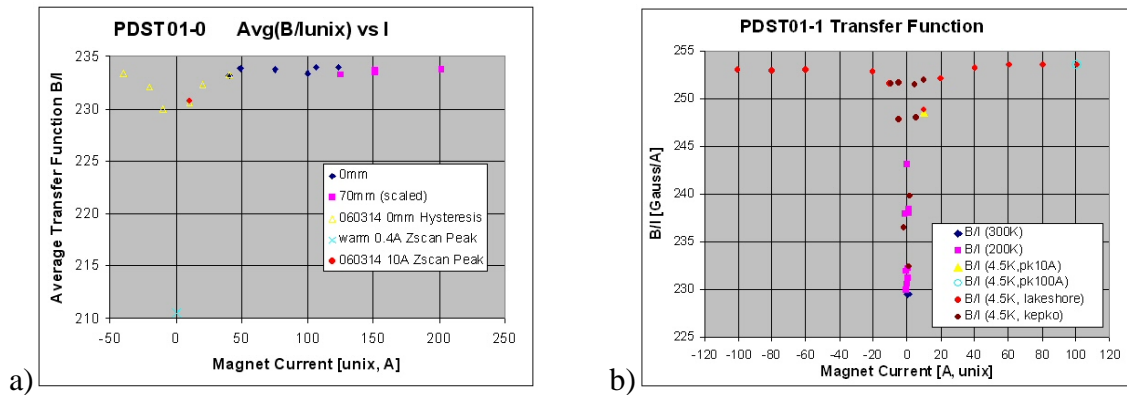


Fig. 20: Transfer function for (a) bare and (b) yoked solenoid.

The plateau values are compared in Table 4 to what the modeling predicts; the comparison shows reasonable agreement.

Table 4. Calculated and Measured Central Field Transfer Function

PDST01 Configuration	Peak Transfer Function, B/I	
	measured	calculated
Bare Coil	233.6 +/- 0.05	~231.5
Yoked Coil	253.5	~250

Investigation of the hysteretic properties of the superconductor, and of the iron yoke, was an important part of the test program for this solenoid. Because of poorly understood behavior of the residual magnetic field, many excitation cycles were made both cold and warm in both configurations to finally clearly identify a *source of hysteresis with the opposite sign* from anything expected to come from the solenoid. This was conjectured to be caused by some ferromagnetic defect in the bore or probe support hardware. Subsequently we determined that four stainless steel mounting screws surrounding the Hall probe were indeed ferromagnetic; in addition, the support plate made of stainless steel also bore residual magnetization. This discovery can qualitatively explain the “wrong-sign” hysteresis, as well as the transfer function deficit at low current. As depicted in Fig. 21, the ferromagnetic defect shunts flux away from the solenoid center at low current, but eventually saturates and so becomes transparent at high current. When the solenoid is off, the residual flux due to this magnetization is directed in the opposite direction, so the Hall probe on the axis of the solenoid registers this “negative” field. This effect obscured our attempts to extract superconductor and yoke hysteresis properties, which therefore were made later for other test solenoids.

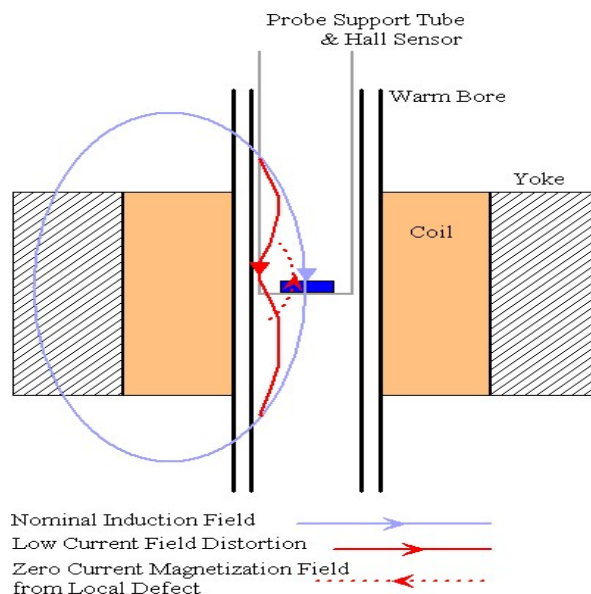


Fig. 21: Qualitative explanation of the “Reverse Hysteresis” effect

Concluding Remarks

As a result of testing the first test solenoid, wound using round SSC strand, the following statements can be made:

1. Maximal magnetic field and the field distribution can be well predicted, for both the bare and the yoked solenoids;
2. Pre-stress features of the solenoid ensure good mechanical stability and help to obtain short training history;
3. The solenoid is self-protected in case of a quench; there is good indication that quench propagation patterns are well understood

A magnetic anomaly in the Hall probe support was found that explains unusual behavior of the transfer function; unfortunately, this prevented measuring the hysteretic properties of the SSC strand in PDST01. However, this problem was solved and hysteresis data were successfully captured for the test solenoids PDST02 and PDST03, which were wound using modified SSC strand and rectangular Oxford strand, respectively. These measurements, in addition to the global properties and quench performance of the solenoids, are reported in separate notes: TD-06-028 and TD-06-029.

References:

- [1] E. Barzi, Error Analysis of the Short Sample J_c Measurements at the Short Sample Test Facility, TD-98-055, FNAL, Sept. 1998
- [2] SSC. Site Specific Conceptual Design, June 1990, pp. 296 - 301
- [3] I. Terechkine, “Solenoid Quench Heater”, TD-06-006, FNAL, Feb. 17, 2006.
- [4] P. Bauer, I. Terechkine, Proton Driver Front End Focusing Solenoid Quench Protection Studies. Part I: Method Description and the First Iteration, TD-06-003, FNAL, Jan. 2006
- [5] I. Terechkine, Proton Driver Front End Focusing Solenoid Quench Protection Studies. Part II: Test Solenoid Quench Protection, TD-06-004, FNAL, Jan. 2006
- [6] I. Terechkine, Test Solenoid Design Proposal, TD-05-040, FNAL, Sept. 2005